Corrosion Science 190 (2021) 109664

Contents lists available at ScienceDirect

Corrosion Science

journal homepage: www.elsevier.com/locate/corsci

Aqueous molybdate provides effective corrosion inhibition of WE43 magnesium alloy in sodium chloride solutions

Dmitry S. Kharitonov [a,*], Małgorzata Zimowska [a], Jacek Ryl [b], Artur Zieliński [c], Maria A. Osipenko [d], Janusz Adamiec [e], Angelika Wrzesińska [f], Per M. Claesson [g,h], Irina I. Kurilo [d]

[a] Jerzy Haber Institute of Catalysis and Surface Chemistry, Polish Academy of Sciences, PL 30-239 Krakow, Poland
[b] Institute of Nanotechnology and Materials Engineering, Faculty of Applied Physics and Mathematics, Gdansk University of Technology, PL 80-233 Gdansk, Poland
[c] Department of Electrochemistry, Corrosion and Materials Engineering, Gdansk University of Technology, PL 80-233 Gdansk, Poland
[d] Department of Physical, Colloid and Analytical Chemistry, Belarusian State Technological University, 220006 Minsk, Belarus
[e] Institute of Materials Science, Silesian University of Technology, PL 40-019 Katowice, Poland
[f] Department of Molecular Physics, Lodz University of Technology, PL 90-924 Lodz, Poland
[g] Division of Surface and Corrosion Science, School of Engineering Sciences in Chemistry, Biotechnology and Health, KTH Royal Institute of Technology, SE 100-44 Stockholm, Sweden
[h] RISE Research Institutes of Sweden, SE 114-86 Stockholm, Sweden

ARTICLE INFO

Keywords:
A. Magnesium
B. EIS
B. XPS
B. Raman spectroscopy
B. Scanning probe microscopy
C. Molybdate inhibitor

ABSTRACT

Corrosion and corrosion inhibition of WE43 magnesium alloy were investigated in NaCl solutions containing different amounts of sodium molybdate. Electrochemical, microscopic, and spectroscopic experiments were utilized to examine the mechanism of corrosion inhibition by molybdates. Electrochemical data showed that Na_2MoO_4 inhibitor provides reliable inhibition at concentrations at and above 100 mM. Raman and XPS spectroscopy demonstrated that the formed surface layer consists of mixed Mo(V, IV) species. This layer provided inhibition with an efficiency of 91–99 % after 24 h of exposure. A two-step oxidation-reduction mechanism of corrosion inhibition of the WE43 alloy by aqueous molybdates was proposed.

1. Introduction

Magnesium alloys are the lightest metallic structural materials widely used in commercial applications. The basic function of alloying elements in Mg alloys is to promote formation of strengthening intermetallic phases (IMPs) that improve desired material properties [1]. The most successful Mg alloys developed to date are Mg-Al-Zn and Mg-Y-RE (rare earth metals) systems [2–4]. Of these, the former have better thermal stability and can be used at moderately elevated temperatures up to 250 °C [5]. The resulting high strength-to-density ratio, good castability, high creep, ignition, and flame resistance made Mg-Y-RE alloys an attractive option for demanding applications in aerospace, automotive, and military sectors [2,5]. However, low standard electrochemical potential (−2.37 V vs. SHE) and high reactivity of Mg cause high susceptibility to corrosion degradation. This characteristic is extensively used in biomedical applications of Mg alloys as biodegradable implants [6,7], yet it is undesirable during industrial use. In the absence of surface protection, weak corrosion resistance significantly limits the range of Mg alloys applications, especially in technically relevant aqueous and non-aqueous media, usually containing chloride ions [8,9]. Moreover, IMPs formed in alloys can increase the susceptibility to localized corrosion due to the microgalvanic interactions with the alloy's matrix [10,11].

There are two major strategies to improve the corrosion resistance of Mg alloys: (*a*) tailoring the composition and microstructure or (*b*) modification of the surface. Even with a notable progress in recent years [12–16], alloying of Mg is still a challenge and does not allow for considerable long-lasting improvement in corrosion resistance. For that reason, development of efficient and environmentally friendly protective schemes would be a benefit. Such a technology can be achieved by combining surface treatment with efficient corrosion inhibitors [17–21].

The protective action of a conventional inhibitor is based on the direct passivation of the metal surface or interaction with the products of metal corrosion, which result in the formation of a passivation layer

* Corresponding author.
E-mail address: Dmitry.Kharitonov@ikifp.edu.pl (D.S. Kharitonov).

https://doi.org/10.1016/j.corsci.2021.109664
Received 28 April 2021; Received in revised form 5 June 2021; Accepted 2 July 2021
Available online 5 July 2021

[17]. In the latter case, an initial pre-corrosion step is required that might be undesirable. For several decades hexavalent chromium compounds were mostly applied to protect Mg alloys from corrosion. Hexavalent chromium is effective but unfortunately highly irritating, toxic, and harmful to the environment [17], making it desirable to replace Cr (VI) with more environmentally benign alternatives.

In recent years, a notable progress in the understanding of inhibiting corrosion of Mg alloys has been achieved [17,18]. Lamaka et al. reported the importance of suppressing cathodic activity of iron impurities or cathodic IMPs, which can act as active sites for hydrogen reduction [22–24]. They also examined the inhibiting effect of 151 individual compounds as potential inhibitors for Mg alloys [20], and proposed sodium salts of pyridinedicarboxylic and salicylic acids as the most efficient and universal inhibitors for Mg alloys. Later, the approach of blocking Fe-rich sites by sulphur was propped in [25]. Based on this, a good inhibitor for Mg-Y-RE alloys should be of mixed nature, suppressing anodic dissolution of the Mg matrix and the cathodic activity of IMPs and noble impurities.

In our previous studies we have shown that aqueous solutions of vanadate and molybdate provided efficient corrosion inhibition of the Al-Mg-Si alloy AA6063-T5, which also contains a high fraction of Fe-rich cathodic IMPs [26–29]. The rapid adsorption of these oxyanions on the alloy matrix and IMPs, which with further reduction results in a protective layer of mixed-valence oxides, suggests their potential effectiveness for Mg alloys. Existing literature reports include significant examinations of permanganate oxyanions as inhibitors of Mg alloys [17,18], while not so much attention has been given to other oxyanions, e.g. vanadate, molybdate, and tungstate. Although, both vanadate and molybdate have been classified as unpromising inhibitors in the report of Lamaka et al. [20], recently the group of Buchheit et al. reported a clear corrosion inhibitive effect of vanadate [30,31] and selenite [32,33] ions for the AZ31 Mg alloy.

A few studies have described the utilization of molybdate together with phosphate or cerium ions for conversion treatment of Mg-Al-Zn [34–39] and Mg-Zn-Y-Zr [40] alloys. In these cases, molybdate was forming stable surface films, which significantly increased the corrosion resistance of the substrate. Since most conversion coatings act by releasing soluble inhibiting species into the aqueous environment, it is of interest to understand the mechanism of inhibition provided by dissolved species [32]. To our best knowledge, no attempt to examine the corrosion protection of Mg-Y-RE alloys by soluble molybdates has been described in the literature. Moreover, correlation of the inhibition mechanism with the microstructure of these alloys still requires a better fundamental understanding. The aim of this study was to elucidate the mechanism of corrosion inhibition provided by aqueous molybdates towards the Mg-Y-RE (WE43) alloy in aqueous NaCl medium, with a specific focus on morphology and phase composition of the metal surface before and after corrosion experiments.

2. Experimental

2.1. Materials and sample preparation

The magnesium alloy WE43 used in this study was prepared as a plate material according to the procedure reported elsewhere [9]. The nominal chemical composition of the alloy is given as (wt.%): 3.7 Y, 2.2 Nd, 0.51 Zr, <0.05 other elements, and balance Mg. The substrate material was cut to specimens with sizes about 10 mm × 10 mm × 5 mm. Before experiments, the samples were mechanically ground to 4000-grit in 99.9 % ethanol. For atomic force microscopy (AFM) and X-Ray photoelectron spectroscopy (XPS) measurements samples were further polished with up to 0.25 μm non-water suspension until a mirror-like surface without visible scratches was achieved. For electrochemical measurements, samples were embedded in epoxy resin with electrical connection on the opposite side of the examined surface.

2.2. Scanning electron microscopy (SEM) and energy-dispersive X-ray (EDX) analyses

The surface morphology and elemental composition of the samples before and after the corrosion experiments were investigated using a JEOL JSM-7500 F Field Emission Scanning Electron Microscope equipped with a retractable backscattered-electron detector (RBEI) and an INCA PentaFetx3 EDX system.

2.3. Scanning probe microscopy (SPM) measurements

Scanning probe microscopy measurements of surface topography and contact Volta potential difference using scanning Kelvin probe force microscopy (SKPFM) were carried out with an NTEGRA Aura (NT-MDT) AFM setup using HQ:NSC18 probes (MikroMasch) with platinum coating. The lift distance for the SKPFM measurements in the second pass was 100 nm. The measurements were conducted in air at ambient conditions and relative humidity of around 50 %. The resulting topography and potential images contain 256 × 256 data points.

2.4. Electrochemical measurements

Electrochemical experiments were carried out using a traditional three electrode setup with a saturated Ag/AgCl reference electrode and a Pt-mesh counter electrode on an Autolab PGSTAT302 N potentiostat/galvanostat. Electrochemical measurements were performed in the following order: electrochemical impedance spectroscopy (EIS), polarization resistance by linear polarization resistance (LPR), and potentiodynamic polarization after 1 and 24 h of exposure to the examined solutions. Different samples were used to perform each series of measurements. The measurements were at least triplicated and the results were recalculated to the surface area of 1 cm^2.

All solutions for corrosion studies were prepared with NaCl (≥99.5) and Na_2MoO_4 (≥99.5) received from Chemsolute (Th. Geyer Polska) and Polwater deionized water with resistivity of 18.2 MΩ cm. Corrosion experiments were performed in 0.05 M NaCl with the concentration of the inhibitor varying in the range of 5–150 mM. The solutions were stored in closed flasks for 24 h under laboratory conditions (~20 °C) to ensure equilibration of Mo species. Reference measurements were done in 0.05 M NaCl without inhibitor.

EIS measurements were carried out at the open-circuit potential (OCP) over the frequency range from 10^5 to 10^{-2} Hz using a sinusoidal perturbation amplitude of 10 mV. The *ZView 3.2c* software was used for data analysis and spectra fitting.

LPR scans were performed in the overpotential range of ±10 mV vs. OCP. The polarization resistance (R_p) was defined as the slope of the potential vs. current density curve based on the Stern-Geary equation:

$$R_p = \frac{\Delta E}{\Delta i_{\Delta E \to 0}}. \quad (1)$$

Potentiodynamic polarization curves were recorded at a scan rate of 0.5 mV/s starting from −200 mV vs. OCP. The measurement was aborted when the polarization reached +500 mV vs. OCP or when the registered current reached 2 mA/cm^2. The *Nova 2.1.4* software was used to extract the electrochemical parameters from the polarization curves.

2.5. Raman spectroscopy

Raman spectra of the WE43 surface were acquired *ex-situ* with a Jobin-Yvon T64000 Raman spectroscopy system using a 514.5 nm laser with incident power of 12 mW. The total acquisition time was 300 s.

2.6. X-ray photoelectron spectroscopy (XPS)

High-resolution XPS spectra were registered directly after exposure to the studied electrolytes for 1 and 24 h using a ThermoFisher Scientific

Escalab 250Xi spectrometer, equipped with an Al K_α X-Ray source (spot size 250 μm), operating at a pass energy of 10 eV. The samples were removed from the solutions, rinsed with deionized water, air dried, and transferred to a vacuum chamber within 5 min. The binding energy values were charge corrected to the carbon C 1s excitation which was set at 284.6 eV. Peak deconvolution was performed in the *Avantage* software.

3. Results and discussion

3.1. Microstructure characterization

The microstructure of as-polished WE43 alloy consists of an α-Mg matrix and numerous eutectic IMPs with different shapes, as shown in Fig. 1. The major fraction of secondary phases has a mesh-type body with sizes around 15–20 μm and rod-shaped laterals of up to 100 μm in length, which is typical for the WE43 alloy [2]. The composition of these IMPs depends on the bulk alloy composition and casting processes [2,41]. Surface elemental EDX maps showed that the formed IMPs are rich in Nd with smaller enrichment of Zr and Y, which are evenly dispersed through the IMP (Fig. 1c). Based on the point EDX analysis the particle is composed of 85.8 at.% Mg, 9.4 at.% Nd, 4.8 at.% Y, and <1 at.% Zr, which is close to the Mg_9Nd_2Y-type IMP.

The electrochemical activity of the IMPs found at the surface of the WE43 alloy was examined using SPM methods. Topography and contact Volta potential difference maps of surface regions containing such IMP are shown in Fig. 2.

The surface topography maps (Fig. 2a) do not show direct evidence of IMPs on the surface. However, the surface of the as-polished alloy is rapidly oxidized even in ambient air, which results in formation of an oxide/hydroxide layer of corrosion products. Some surface precipitates indicated in Fig. 2a, b were protruding from the surface by hundreds of nanometers and can be remnant particles of the polishing suspension. The height profiles presented in Fig. 2c show height fluctuations of typically about 50 nm, with some reaching 200 nm over the corrosion-induced precipitates.

The SKPFM measurement is a useful tool to predict and understand the local micro–galvanic corrosion propensity of metals [29,42–44]. A linear relation between the Volta potential measured in air and the corrosion potential in aqueous solutions [42] can be used to assign surface regions in the material as being preferentially anodic or cathodic. Some intermetallic particles are clearly visible in the SKPFM Volta potential map since they have a different contact potential difference compared to the alloy matrix, see Fig. 2b. In the galvanic couple IMP-Mg matrix, the matrix will serve as the anode due to its lower Volta potential [11,45]. Thus, it can be expected that in the case of galvanic corrosion, local corrosion will be initiated at the IMP/matrix interface and will procced towards the alloy matrix. The surface potential profiles (Fig. 2d) revealed a Volta potential difference of ~60 mV for the large IMP (profile *1*) and ~50 mV for the smaller one (profile *3*) relatively to Mg matrix. These values are two-three times larger than those previously reported for Mg-Nd-Y IMPs [46]. This can be explained by a lower fraction of anodic component (Mg) in the Mg_9Nd_2Y-type IMPs found in the examined alloy as compared to the Mg_{12}(Nd,Y) phases in [46].

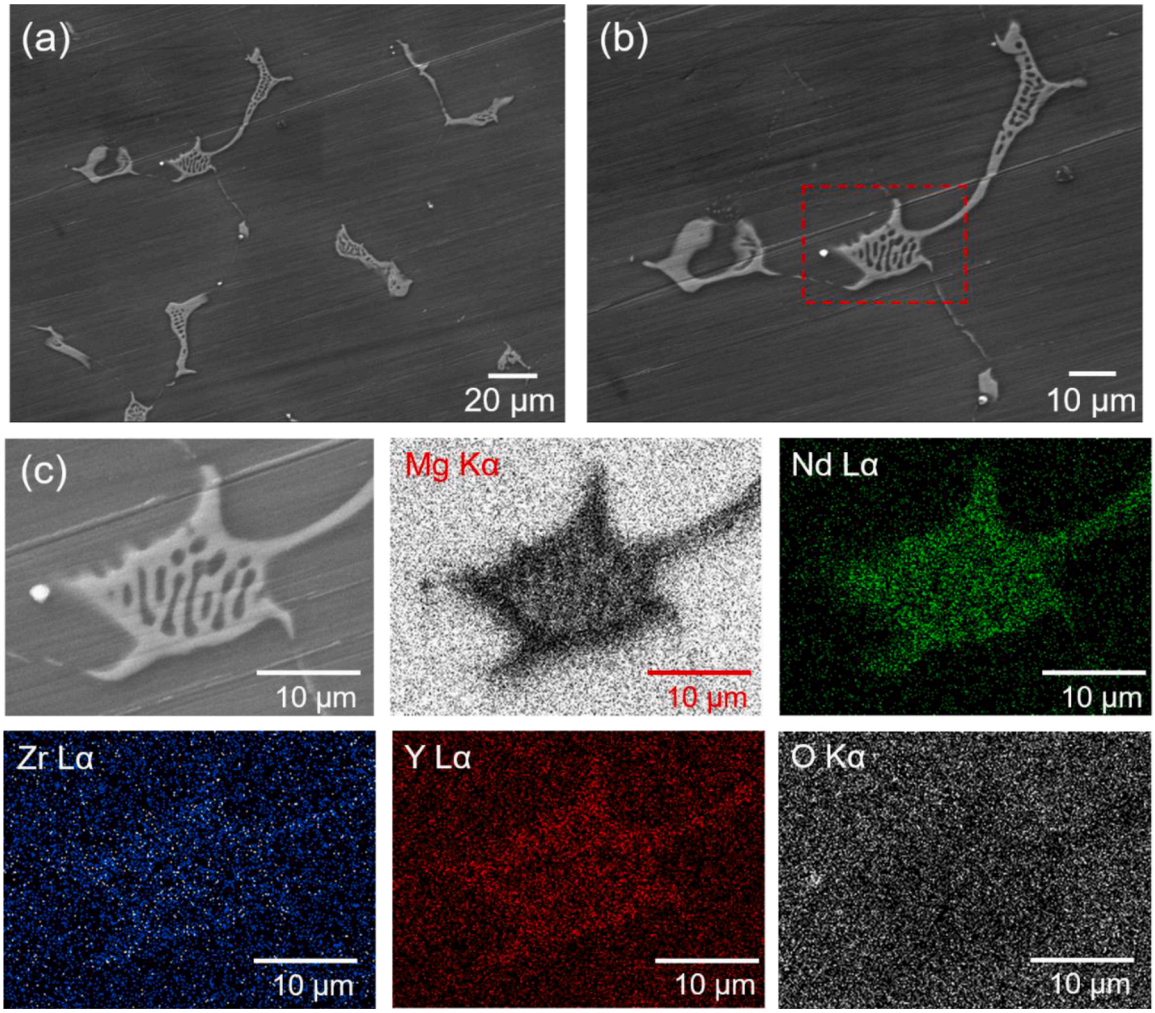

Fig. 1. SEM images of as-polished WE43 surface (a, b) and EDX maps (c) showing elemental distribution over the surface region marked in (b).

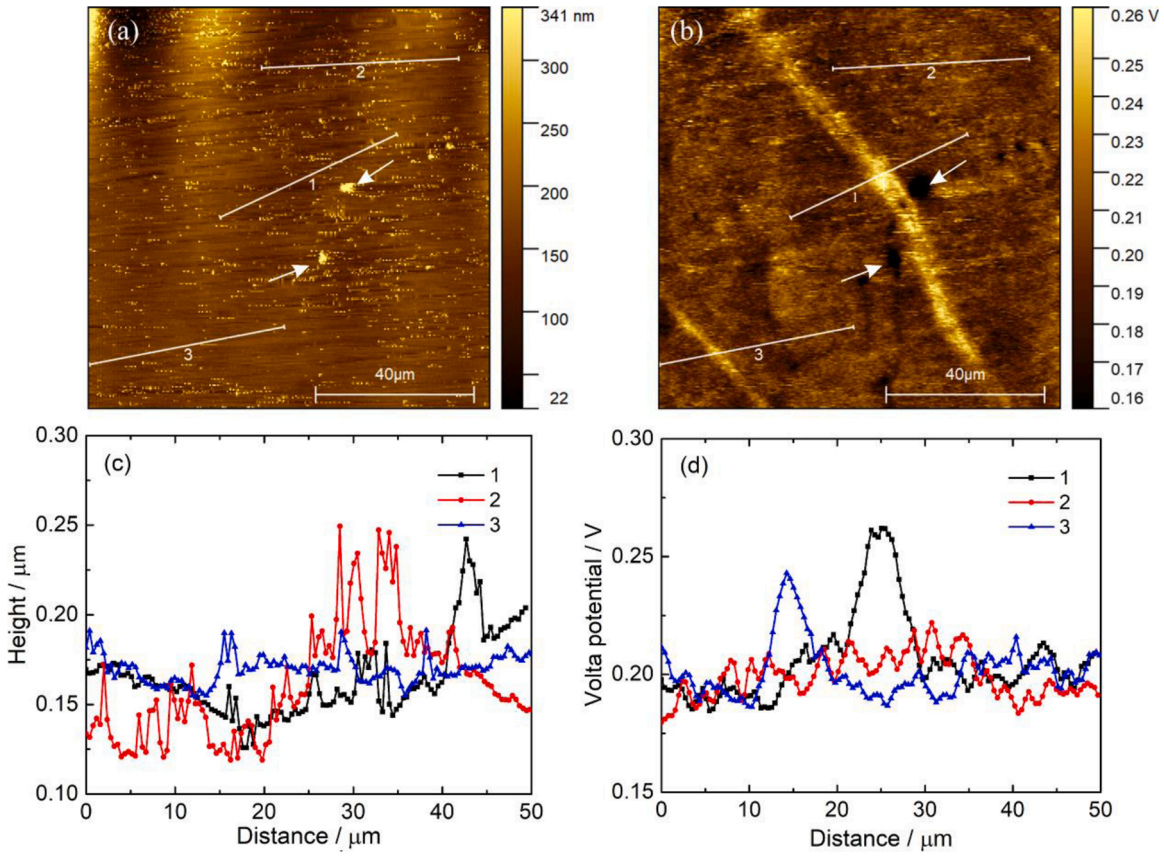

Fig. 2. Topography AFM map (a) and corresponding SKPFM Volta-potential map (b) of a WE43 alloy surface. Line profiles show the topography (c) and Volta-potential (d) along the lines in the corresponding maps (a, b). The image size was 100 × 100 μm^2. Arrows in (a, b) indicate surface precipitates.

Fluctuations of the Volta potential over the surface of the Mg matrix do not exceed 20 mV and are suggested to be caused mainly by the inhomogeneous layer of atmospheric corrosion products on the surface.

3.2. Electrochemical evaluation of corrosion inhibition by molybdate

The corrosion properties of the WE43 alloy at different molybdate concentrations in 0.05 M NaCl solution were evaluated by a set of electrochemical measurements, coupled with SEM/EDX observations.

3.2.1. Potentiodynamic polarization

The OCP was followed for 1 h under each condition. The OCP profiles of the WE43 alloy monitored for 1 h after immersion in 0.05 M NaCl with varying concentrations of dissolved Na_2MoO_4 are shown in Fig. 3. In the 0.05 M NaCl solution without inhibitor the OCP of the WE43 alloy gradually increased from –(1.67 ± 0.08) V to –(1.51 ± 0.12) V. In the presence of the molybdate inhibitor, the OCP evolved differently over time. At the outset of the exposure, the OCP value shifted in the cathodic direction up to ca. –1.50 V (5 and 10 mM/L of added Na_2MoO_4) and –1.42 V (50–150 mM/L of added Na_2MoO_4), suggesting rapid adsorption of molybdate on the surface of the WE43 alloy. The OCP in the solution containing 5 mM Na_2MoO_4 was rapidly increasing during the first minutes of the experiment and then stabilizing at about −1.43 V with small but distinct fluctuations. Further increase in the amount of added inhibitor did not significantly change the trend of the OCP variation with time: a rapid OCP increase during the first 10 min followed by potential stabilization without prominent fluctuations. The value of the stabilized OCP increased with increasing molybdate concentration and reached ca. –1.26 V in the 150 mM Na_2MoO_4 + 0.05 M NaCl solution. The OCP profiles suggest that at high concentrations the molybdate inhibitor rapidly forms a stable film, which shifts the corrosion potential in the noble direction.

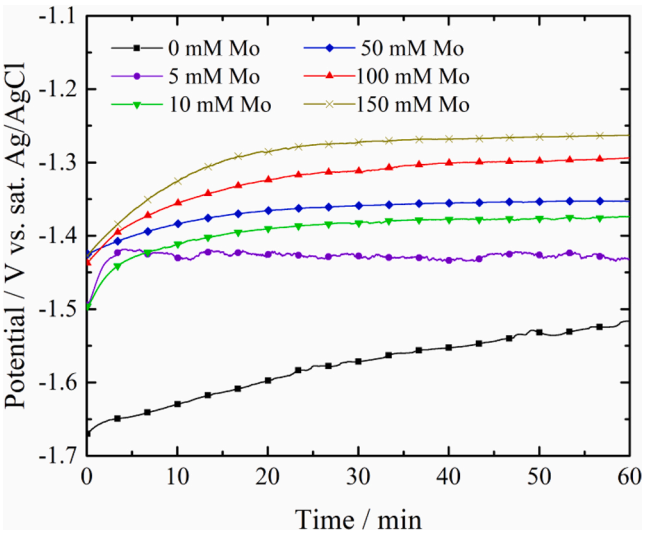

Fig. 3. Time-dependent open-circuit potential (OCP) of the WE43 alloy in 0.05 M NaCl solutions containing various amounts of Na_2MoO_4 inhibitor.

Potentiodynamic polarization curves obtained after 1 and 24 h of exposure in 0.05 M NaCl solutions with different concentrations of the molybdate inhibitor are shown in Fig. 4. The results of the measurement in absence of inhibitor revealed, as expected, that the WE43 alloy has a poor corrosion resistance under such conditions. Both the cathodic and anodic branches of the polarization curves showed an active response with the corrosion current density, i_{corr}, determined by Tafel extrapolation, of (4.1 ± 1.4) × 10^{-5} A/cm^2 and (7.2 ± 0.8) × 10^{-5} A/cm^2 after 1

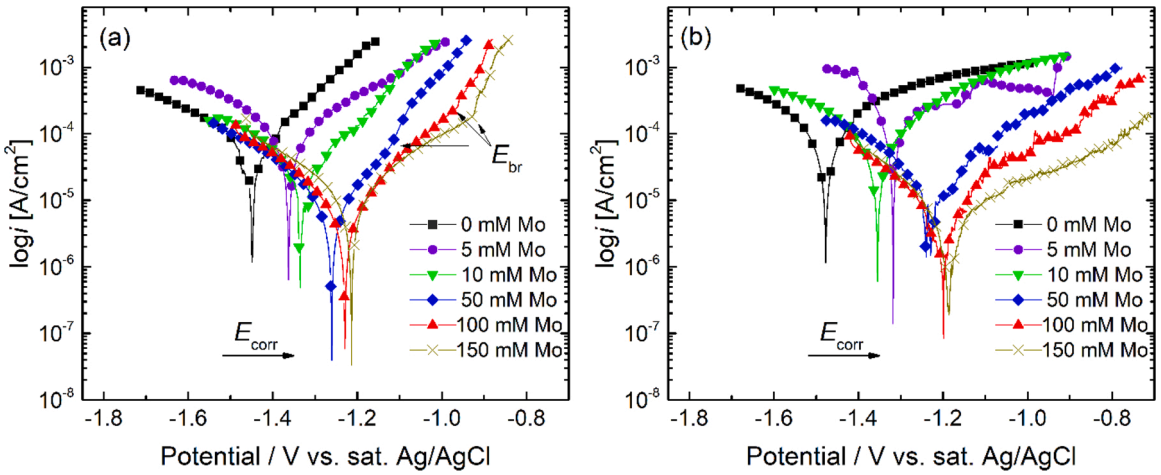

Fig. 4. Potentiodynamic polarization curves obtained after 1 h (a) and 24 h (b) exposure in 0.05 M NaCl without and with molybdate inhibitor. The scale in (a) and (b) is the same for the ease of comparison. The scan direction was from the cathodic to the anodic branch.

and 24 h of exposure, respectively (Table 1). The polarization curves obtained in molybdate-containing NaCl solutions showed a notable change in the kinetics of the anodic processes. A gradual decrease in i_{corr} was observed with increasing molybdate concentration. The corrosion potential, E_{corr}, gradually increased, following the trend of the OCP. The largest inhibitory effect was observed at 100 and 150 mM of added Na_2MoO_4, for which the value of i_{corr} decreased by an order of magnitude and E_{corr} increased by ca. 190−200 mV compared to the situation without inhibitor. This was the case for the WE43 samples exposed for both 1 and 24 h. Furthermore, starting from 50 mM of added Na_2MoO_4 it was possible to mark the breakdown potential, E_{br}, on the anodic branches of the polarization curves recorded after 1 h of corrosion. This provides evidence for the presence of a protective layer on the WE43 alloy surface under these conditions.

Small-amplitude LPR scans performed in the overpotential range of ±10 mV vs. the OCP under the same experimental conditions showed gradual increase in the R_p values with increasing inhibitor concentration up to 100 mM. However, the addition of 150 mM Na_2MoO_4 to 0.05 M NaCl solution resulted in a noticeable decrease in R_p (Table 1). Using the values of i_{corr} and R_p extracted from the potentiodynamic results in NaCl solutions without and with the molybdate inhibitor it is possible to evaluate the inhibition efficiency, *IE*, which was calculated as:

$$IE_1 = [1 - (i_{corr}/i^0_{corr})] \times 100\%, \quad (2)$$

$$IE_2 = [1 - (R^0_p/R_p)] \times 100\%, \quad (3)$$

where i^0_{corr}, R^0_p and i_{corr}, R_p are the corrosion current densities and polarization resistances in the absence and presence of the inhibitor, respectively. The highest *IE* was reached in the solutions containing 100 and 150 mM of Na_2MoO_4 (Table 1).

3.2.2. *Electrochemical impedance spectroscopy*

The results of EIS measurements of the WE43 alloy in 0.05 M NaCl solution without and with inhibitor are shown in Fig. 5. The Nyquist plot of the WE43 alloy in 0.05 M NaCl solution without inhibitor (Fig. 5a) characteristically displays one large capacitive loop at high frequencies, a smaller depressed capacitive loop at medium to low frequencies, and an inductive loop at low frequencies. Such a frequency response of the electrical impedance for Mg alloys in NaCl solutions has previously been reported in several studies [47–49]. In this case, the inductive property is typically associated with relaxation processes of adsorbed intermediates of the corrosion process [47,49–53]. However, their exact nature is still debated [47] and requires further analysis.

The impedance of the WE43 alloy was observed to increase in inhibitor-containing 0.05 M NaCl solutions after both 1 and 24 h (Fig. 5b,c). Typically, the amplitude of the low-frequency capacitive loop, corresponding to the impedance of the WE43 surface, increased significantly and indicated improved corrosion resistance. A low-frequency inductive response was also clearly visible, except for the case of 24 h in solutions containing 100 and 150 mM of Na_2MoO_4, where only the capacitive response was registered (Fig. 5c). That is explained by the blocking effect of the inhibitor layer and corrosion products

Table 1
Electrochemical parameters with standard deviation of three measurements extracted from potentiodynamic polarization measurements in 0.05 M NaCl solutions with varying concentration of Na_2MoO_4 inhibitor.

$C(Na_2MoO_4)$ /mM	E_{corr}/V	i_{corr}/A/cm^2	IE_1/%	R_p/Ω cm^2	IE_2/%
1 h of immersion					
0	–1.410 ± 0.052	(4.1 ± 1.4) × 10^{-5}	–	672 ± 40	–
5	–1.334 ± 0.025	(2.3 ± 1.3) × 10^{-5}	56	1081 ± 45	38
10	–1.307 ± 0.031	(8.1 ± 1.8) × 10^{-6}	84	2033 ± 118	67
50	–1.234 ± 0.030	(6.4 ± 0.7) × 10^{-6}	87	2912 ± 359	77
100	–1.221 ± 0.014	(4.6 ± 0.5) × 10^{-6}	91	3363 ± 167	80
150	–1.206 ± 0.007	(7.2 ± 0.6) × 10^{-6}	86	2567 ± 241	73
24 h of immersion					
0	–1.477 ± 0.095	(7.2 ± 0.8) × 10^{-5}	–	456 ± 29	0
5	–1.318 ± 0.044	(1.1 ± 0.9) × 10^{-4}	–57	214 ± 18	–113
10	–1.355 ± 0.015	(5.3 ± 1.4) × 10^{-5}	26	489 ± 89	7
50	–1.243 ± 0.102	(8.9 ± 1.5) × 10^{-6}	87	1946 ± 219	77
100	–1.199 ± 0.091	(3.6 ± 0.8) × 10^{-6}	95	5626 ± 326	92
150	–1.187 ± 0.073	(4.0 ± 0.5) × 10^{-6}	94	5358 ± 489	91

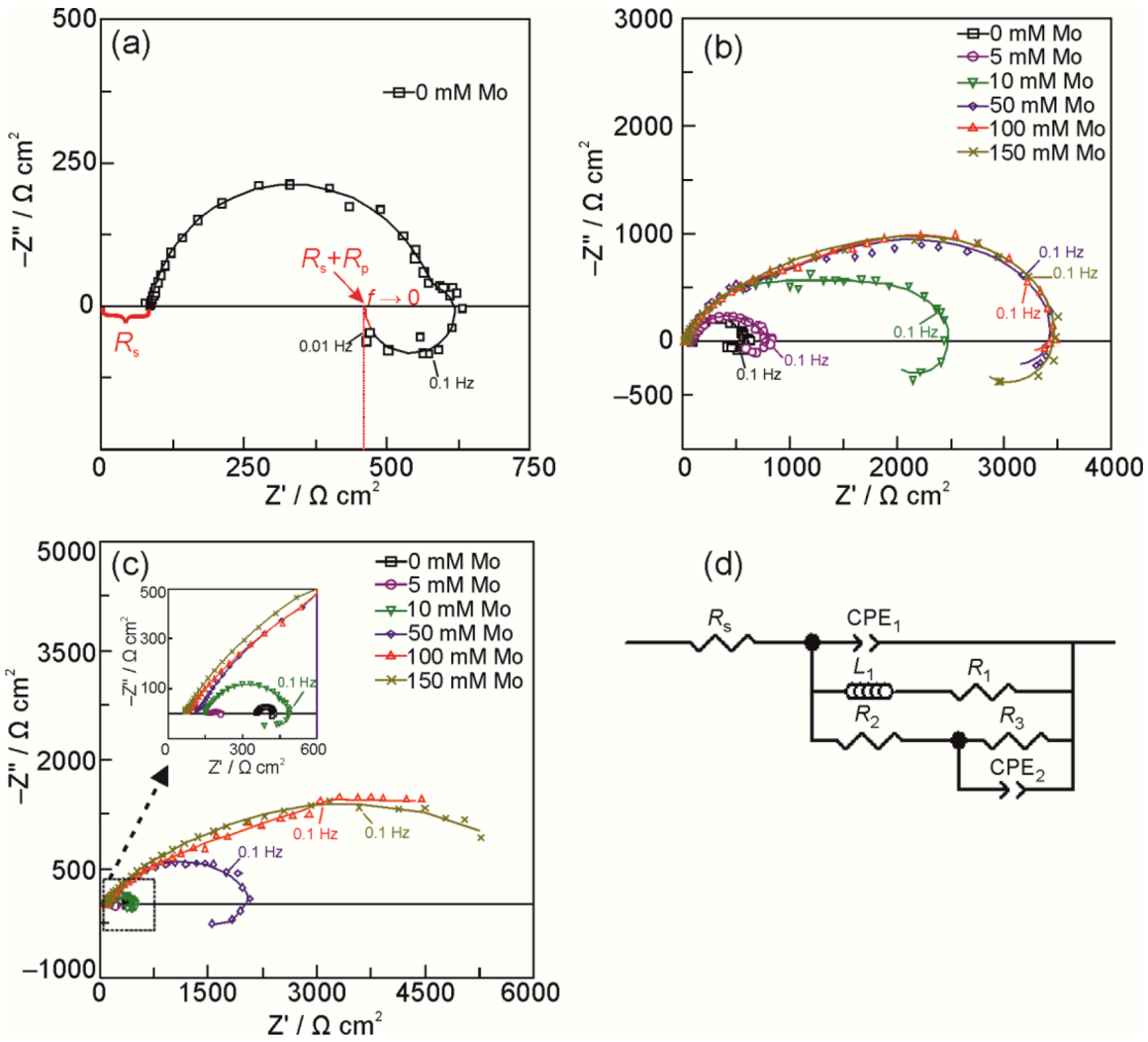

Fig. 5. Nyquist EIS plots in 0.05 M NaCl solution without and with varying amounts of Na_2MoO_4 inhibitor after 1 h (a, b) and 24 h (c) of exposure. The symbols represent experimental data and the lines are results of curve fitting using the equivalent circuit (d).

adsorbed on the alloy surface, which suppress the active dissolution of the alloy. EIS spectra recorded after 24 h exposure to 0.05 M NaCl solution without inhibitor and with 5 mM of molybdate were highly distorted (Fig. 5c), due to pronounced corrosion attack.

The EIS data were analyzed and fitted following the approach proposed in [47]. To minimize the possible overestimation of the corrosion resistance, the inductive response at low frequencies was taken into account in all spectra. The equivalent circuit used for spectra fitting is shown in Fig. 5d. In this circuit, R_s is the solution resistance, CPE_1 represents the capacitance response of the surface film, L_1 and R_1 are the inductance and resistance parameters involving adsorbed intermediates that give rise to the impedance response at low frequencies, R_2 is the surface film resistance, CPE_2 represents the double-layer capacitive response, and R_3 is the charge transfer resistance [47,49,54]. Before fitting, the data reliability was evaluated using Kramers–Kronig transform test proposed by Boukamp [55] with the χ^2-distribution quality usually better than 10^{-3}. The quantitative assessment of *IE* in this case was performed based on the R_p values using Eq. (3). From EIS spectra, R_p can be estimated as the difference between the solution resistance (R_s) and the low-frequency intersection of the total impedance with the abscissa. This approach is graphically illustrated in Fig. 5a. In this case, after fitting experimental data with the proposed circuit (Fig. 5d) in the measured frequencies range, the fitted data were extrapolated to lower frequencies. On the other hand, for the used equivalent circuit R_p can also be calculated as:

$$\frac{1}{R_p} = \frac{1}{R_1} + \frac{1}{R_2 + R_3}. \quad (4)$$

Here it is assumed that the capacitive response of the measured system approaches infinite impedance and the inductive response approaches zero as the measurement frequency tends towards zero [47]. The difference in R_p values obtained by these two approaches did not exceed 0.2 Ω. Note that *IE* was calculated based on Eq. (4), not from graphical extrapolation. The obtained fit parameters and calculated R_p and *IE* values are summarized in Table 2.

The lowest value of R_p was found for WE43 in 0.05 M NaCl solution without inhibitor. In molybdate-containing solutions, R_p increased gradually with concentration, except for the case when 150 mM Na_2MoO_4 were added.

Summarizing the results of the electrochemical measurements, it is clearly seen that R_p and *IE* values in all cases suggest significant corrosion inhibition by molybdates at high (50–150 mM) concentrations. However, the exact values determined under the same experimental conditions but by different electrochemical methods showed some discrepancy, especially in solutions containing 5–10 mM of molybdate inhibitor. This arises from the different nature of the measured parameters. Another reason may come from the used measurement procedure. Experimental data were obtained from the surface of a sample in the following order: EIS → LPR(R_p) → potentiodynamic polarization. The

Table 2
Fitting data with standard deviation of three measurements and calculated inhibition efficiency (*IE*) extracted from EIS measurements.

$C(Na_2MoO_4)$/ mM	R_s/Ω cm^2	R_1/kΩ cm^2	$Y_1\times 10^6$/Ω^{-1} cm$^{-2}s^n$	n_1	R_2/Ω cm^2	$Y_2\times 10^4$/Ω^{-1} cm$^{-2}s^n$	n_2	L_1/kH cm^2	R_3/Ω cm^2	R_p/Ω cm^2	*IE*/ %
1 h of immersion											
0	86.9 ± 0.8	1.2 ± 0.1	15.3 ± 0.9	0.90 ± 0.01	494.2 ± 8.5	66.3 ± 28.8	0.93 ± 0.03	6.1 ± 1.1	52.5 ± 22.7	374.6	–
5	78.9 ± 0.8	4.7 ± 1.9	28.5 ± 5.4	0.81 ± 0.02	568.7 ± 198.4	10.7 ± 1.2	0.88 ± 0.05	17.4 ± 2.8	201.0 ± 26.9	661.6	43
10	67.5 ± 1.8	5.0 ± 0.7	31.8 ± 2.8	0.82 ± 0.01	1182.0 ± 149.0	4.7 ± 0.5	0.79 ± 0.03	55.9 ± 16.3	1783.1 ± 396.7	1385.7	80
50	33.4 ± 1.2	12.7 ± 2.9	30.3 ± 2.0	0.81 ± 0.01	1125.5 ± 182.3	2.1 ± 0.2	0.77 ± 0.03	74.7 ± 5.4	2692.0 ± 313.8	2306.9	87
100	21.5 ± 0.4	21.2 ± 3.3	44.9 ± 2.7	0.74 ± 0.03	1607.8 ± 264.1	2.5 ± 0.1	0.74 ± 0.03	12.0 ± 3.8	2145.4 ± 92.2	3189.4	88
150	20.6 ± 1.1	7.1 ± 1.2	36.8 ± 1.5	0.79 ± 0.02	951.3 ± 128.3	2.0 ± 0.1	0.74 ± 0.04	11.3 ± 1.9	3402.2 ± 109.3	2698.7	86
24 h of immersion											
0	256.1 ± 5.7	0.2 ± 0.06	42.6 ± 6.6	0.99 ± 0.01	28.1 ± 7.1	74.6 ± 14.9	0.99 ± 0.01	3.6 ± 0.7	40.3 ± 7.5	53.2	–
5	175.9 ± 2.6	0.5 ± 0.1	60.1 ± 5.4	0.82 ± 0.02	22.5 ± 6.4	51.2 ± 9.0	0.92 ± 0.05	7.9 ± 0.8	32.9 ± 18.4	50.2	–6
10	147.3 ± 1.6	0.9 ± 0.1	79.5 ± 7.2	0.86 ± 0.01	209.7 ± 49.4	20.4 ± 1.5	0.99 ± 0.01	8.3 ± 0.6	132.6 ± 49.8	244.8	78
50	101.9 ± 2.2	4.7 ± 1.6	25.8 ± 5.6	0.90 ± 0.10	114.1 ± 14.5	7.6 ± 0.5	0.86 ± 0.03	75.5 ± 26.5	1880.6 ± 45.2	1399.5	96
100	71.4 ± 1.2	25.2 ± 0.4	23.2 ± 0.9	0.72 ± 0.03	2342.2 ± 325.1	5.3 ± 0.9	0.74 ± 0.12	7.5 ± 1.8	4915.4 ± 155.2	5634.3	99
150	66.85 ± 1.8	21.4 ± 0.1	83.3 ± 3.1	0.68 ± 0.01	1899.9 ± 453.6	2.5 ± 0.1	0.69 ± 0.07	8.3 ± 2.3	3352.2 ± 161.7	4216.3	98

total duration of the measurement was around 30 min that may also affect the reported inhibitor efficiency. Based on the electrochemical experiments, a concentration of 100 mM of the Na_2MoO_4 inhibitor was selected as the most promising, and it was used in further experiments.

3.3. Post-corrosion surface analysis

To further understand the mechanism of the inhibition action of molybdate, free exposure corrosion experiments in 0.05 M NaCl solution without and with 100 mM of the molybdate inhibitor were performed, and the surface morphology as well as the surface film composition were analyzed.

3.3.1. Surface morphology

SEM micrographs of the WE43 surface after 1 and 24 h of exposure to 0.05 M NaCl solution are shown in Fig. 6. Two characteristic surface regions can be distinguished after 1 h in NaCl solution (Fig. 6a–f). The first region (Fig. 6a–c) is characterized by general corrosion of the surface with some local corrosion attack in the periphery of IMPs marked with an arrow in Fig. 6b. Simultaneously, some regions of the surface have undergone especially severe corrosion attack already after 1 h (Fig. 6d–f). In this case, numerous areas of pitting corrosion of the alloy matrix (marked with arrows) with a thick layer of corrosion products covering the surface were detected. After 24 h of exposure, the whole surface of the sample was covered with a thick, uneven layer of corrosion products with some clearly seen globular particles on the top. The results of the point EDX analysis (marked with * in Fig. 6h) showed that these regions are rich in Mg (38–44 wt.%), O (35–55 wt.%), and Cl (0.8–4.2 wt.%), supporting deposition of an oxide-hydroxide layer of corrosion products on the surface.

Fig. 7 shows the surface morphology of the WE43 alloy after immersion in 0.05 M NaCl with 100 mM of the molybdate inhibitor. In this case the surface morphology was clearly different with almost the whole surface covered by a passivating Mo-containing layer already after 1 h of exposure. Evidently, the thickness of this layer appears to be larger over the alloy matrix than over IMPs, and outlines of single IMPs can be easily distinguished (Fig. 7b,c). Numerous cracks observed in the passive layer are most probably caused by internal stress originating from the drying of the samples upon their removal from the test solution. This feature is well-known for thick passivating layers [38,56]. Some round-shaped non-covered surface regions seen in Fig. 7b are caused by hydrogen bubbles, generated due to corrosion attack during the first minutes of immersion and adsorbed on the surface. The surface coverage of the Mo-based layer increased after 24 h with an almost homogeneous distribution even over IMPs (Fig. 7d–f). Some flakes of the passivating layer were observed to partially exfoliate from the alloy surface. This may be attributed to an action of hydrogen bubbles formed on the metal/passive layer interface due to the corrosion attack initiated in the defects of the passive layer. Nevertheless, this exfoliation will not result in permanent loss of corrosion protection as molybdate ions in the solution will readily form a new protective layer.

The point EDX analysis (areas marked with * in Fig. 7e) showed that the surface layer is primarily composed of Mg (15–36 wt.%), O (28–47 wt.%), and Mo (6–35 wt.%). The relative Mo/O ratio cannot be estimated reliably from the EDX data since the surface layer also contains hydrated Mg compounds with varying stoichiometry [57]. However, our data clearly show that the molybdate inhibitor is able to form a surface layer on the WE43 alloy surface.

3.3.2. Raman spectroscopy

To further understand the mechanism of corrosion inhibition provided by molybdate, Raman spectra were acquired from the typical surface areas marked in Fig. 8. Raman spectra of the WE43 surface after exposure to 0.05 M NaCl for 1 h and 24 h are presented in Fig. 9a. The evolution of surface corrosion products during Mg corrosion using Raman spectroscopy was reported in a series of works by Volovitch et al. based on the Raman peak at 3652 cm^{-1} corresponding to the A_{1g} O—H stretching vibrations in $Mg(OH)_2$ [58–60]. In our experiments, the surface films of corrosion products were rather thick, and spectra were acquired *ex situ*. Moreover, the main Raman peaks of Mo-based compounds are located below 1200 cm^{-1}. For these reasons, analysis of Mg-containing corrosion products was performed focusing on the low-wave number region (200–1100 cm^{-1}). Spectra recorded after 1 h (Fig. 9a, spectrum *1*) and 24 h (Fig. 9a, spectra *2* and *3*) of exposure to

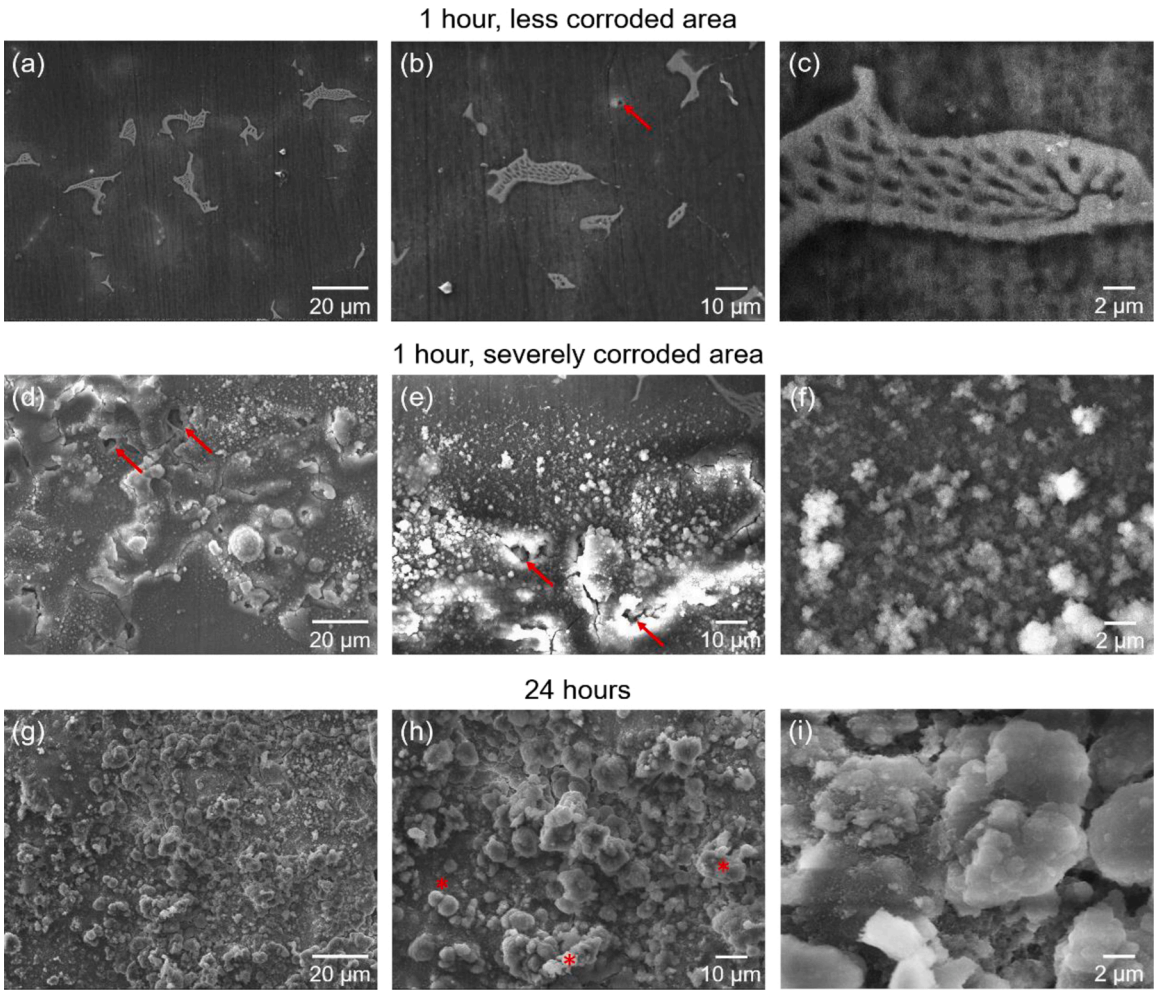

Fig. 6. SEM images of the WE43 surface after 1 h (a–f) and 24 h (g–i) exposure to 0.05 M NaCl solution. Arrows indicate local corrosion attack sites and markers * indicate regions of point EDX analysis.

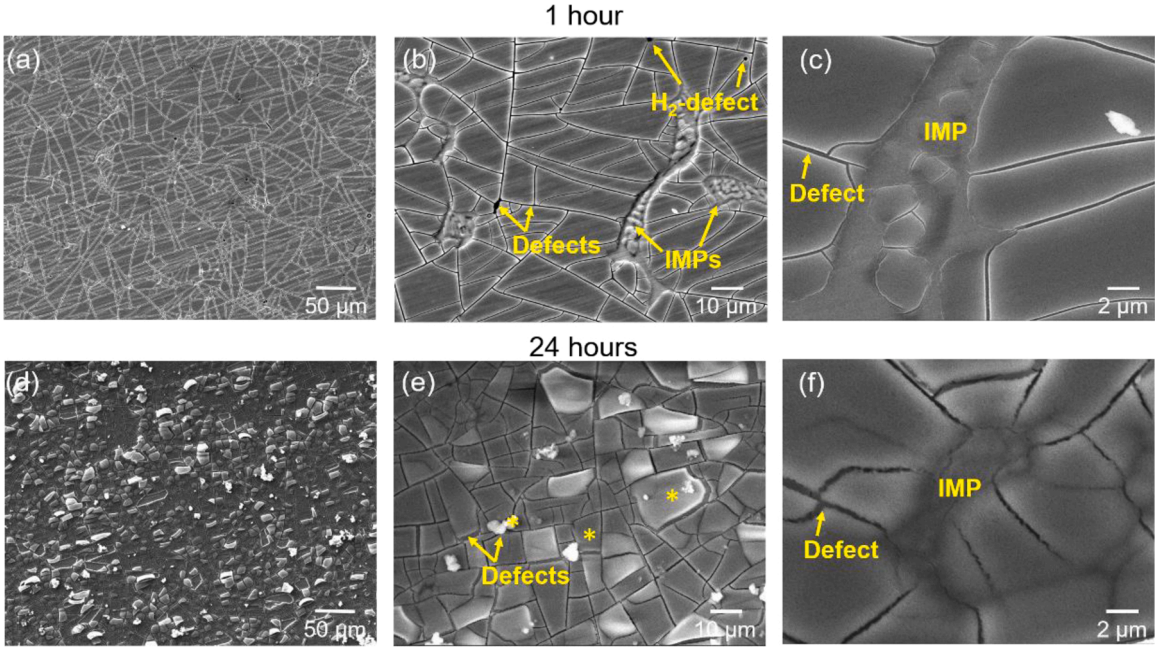

Fig. 7. Surface morphology of the WE43 alloy after 1 and 24 h exposure to 0.05 M NaCl solution with 100 mM Na_2MoO_4. Markers * in (e) show regions of point EDX analysis.

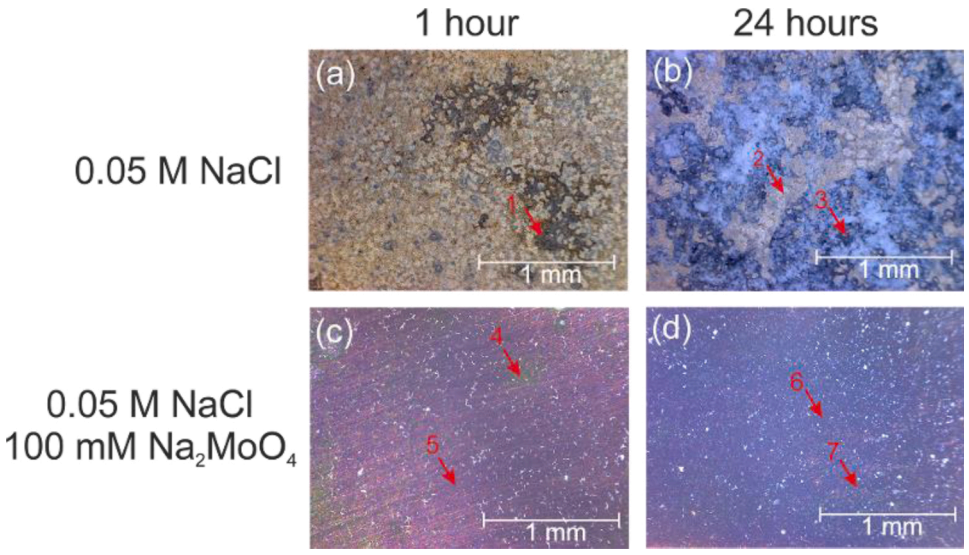

Fig. 8. Light microscopy images of the WE43 alloy surface after 1 and 24 h exposure to 0.05 M NaCl solution without (top row) and with (bottom row) 100 mM of Na_2MoO_4 inhibitor. Arrow markers show regions of Raman analysis.

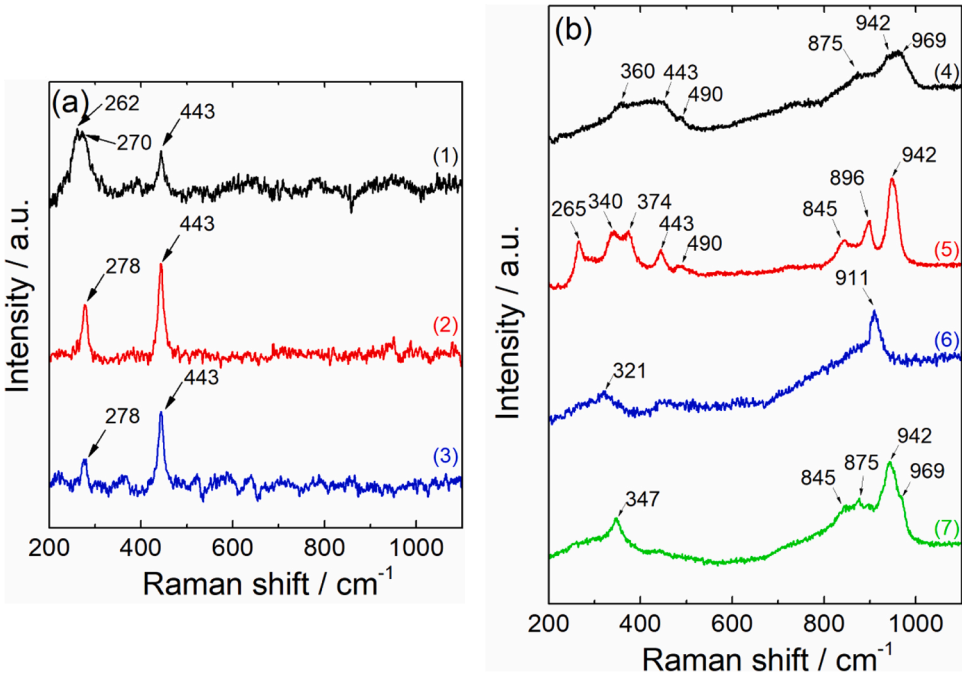

Fig. 9. Raman spectra of the WE43 surface after 1 h and 24 h exposure to 0.05 M NaCl solution without (a) and with (b) 100 mM Na_2MoO_4. The spectra numbers correspond to the surface areas marked in Fig. 8.

0.05 M NaCl demonstrated Raman bands at 443 cm^{-1} (A_{1g}) and 262–278 cm^{-1} (E_g) as typical for $Mg(OH)_2$ [61].

Raman spectra recorded on the WE43 surface after corrosion experiments in 0.05 M NaCl solutions with 100 mM of molybdate inhibitor are shown in Fig. 9b. Molybdenum compounds can form various complexes in different oxidation states [62] and interpretation of Raman peaks should be done with caution. Therefore, the position of the ν_{sym} (Mo–O) band in the range 880–1000 cm^{-1} was analysed for the species assignment due to its sensitivity to changes in the coordination geometry, the chain length, and hydration degree of molybdate species [63]. This approach was also utilized in our previous publication [29]. Typical Raman band positions of solid and aqueous molybdenum species used for spectra interpretation are summarized in our previous work [29]. Two typical spectra were recorded after 1 h of exposure. Both spectra have a Raman band centered at 443 cm^{-1}, which was assigned to Mg $(OH)_2$ [61]. Spectrum recorded at a light-coloured surface spot (Fig. 9b, spectrum *4*) shows low-intense wide bands associated with molybdates with maxima located at 969, 942, 875, 490, and 360 cm^{-1}. Bands at 969 and 942 cm^{-1} were identified as ν_{sym} (Mo–O) bands of hydrated polymolybdates $Mo_7O_{24}^{6-}$ and $Mo_8O_{26}^{4-}$, respectively [63]. The band at 875 cm^{-1} was assigned to the stretching mode of a Mo–O–Mo bond in $Mo_8O_{26}^{4-}$ species [64]. The nature of the peaks at 490 and 360 cm^{-1} is not so evident. These peaks are typical for reduced molybdenum species, mainly in the form of MoO_2 [63]. However, no evidence for the most intensive Raman bands of Mo(IV) in the region 700–800 cm^{-1} was seen in the spectrum. Thus, these bands were attributed to the asymmetric stretching (490 cm^{-1}) and bending (360 cm^{-1}) of the terminal Mo = O

bonds in polymolybdates $Mo_7O_{24}^{6-}$ and $Mo_8O_{26}^{4-}$ [63,65]. The shape of the Raman peaks and their small intensity suggest that the protective layer initially formed on the WE43 surface consists of distorted hydrated molybdenum structures.

The Raman spectrum registered in a darker surface area (Fig. 9b, spectrum *5*) showed strong Raman bands at 942, 896, 845, 490, 374, 340, and 265 cm^{-1}, typical of crystalline molybdates [64]. As before, the bands at 942 and 490 cm^{-1} were assigned to $Mo_7O_{24}^{6-}$. Raman bands at 896, and 845 cm^{-1} were identified as the symmetric and asymmetric stretching of the terminal Mo = O bonds in MoO_4^{2-} molybdate [56,63,64]. The assignment of the remaining bands is rather speculative. Their frequencies are slightly shifted due to the distortion of the surface molybdate compounds [29,63,64]. Another reason can be partial reduction of Mo(VI) species to mixed-valence Mo(VI)–Mo(V) compounds. However, no reliable evidence for this was found in the literature. Therefore, based on the ν_{sym} (Mo–O) band analysis, these bands were tentatively assigned to $Mo_7O_{24}^{6-}$ and MoO_4^{2-} compounds.

After 24 h of exposure, two typical appearances of the Raman spectra were registered on the WE43 surface (Fig. 9b, spectra *6* and *7*). Spectrum *6* contains only two prominent Raman bands at 911 and 321 cm^{-1}. These bands originate from solid dimolybdates $Mo_2O_7^{2-}$ [65]. Spectrum *7* is similar to those registered after 1 h of exposure. The main Raman band at 942 cm^{-1} and smaller band at 875 cm^{-1} originate from $Mo_7O_{24}^{6-}$. A small shoulder band at 969 cm^{-1} is the signal from $Mo_8O_{26}^{4-}$, while MoO_4^{2-} was observed at 845 cm^{-1}. The higher intensity of the peaks suggests that a thicker and more crystalline Mo-containing layer was formed after 24 h compared to the sample exposed to the solution for 1 h. The absence of Raman bands at 990–1050 cm^{-1} demonstrates that pure oxides, like MoO_3 or Mo_4O_{11}, are not present on the surface. To summarize, Raman analysis suggests that corrosion inhibition of the WE43 surface is predominantly provided by a layer of Mo(VI) mono- and polyoxomolybdates. Importantly, there are no Raman peaks assigned to reduced phases of Mo(IV) compounds.

3.3.3. XPS spectroscopy

To further analyze the chemical state of Mo on the surface of the WE43 alloy after corrosion experiments, high-resolution XPS spectra in the binding energy range of Mo3*d* were acquired (Fig. 10). The spectra were deconvoluted into two peak doublets corresponding to electronic states: Mo(VI) compounds ($Mo_{(1)}$ component) and Mo(V) compounds ($Mo_{(2)}$ component) [29,63]. The absence of the peak doublet characteristic for Mo(IV) compounds at 229.2 eV supports the assumptions made during analysis of the Raman data that no such compounds are present. Further, even though Raman analysis did not clearly show the presence of Mo(V) species, such species are present in the top few nanometers of the surface as demonstrated by the XPS analysis. The relative Mo(V) : Mo(VI) ratio was 1.0 : 1.1 and 1.0 : 2.7 after 1 h and 24 h of exposure to the solution, respectively. It indicates that the amount of Mo(VI) species in the surface layer increases with time.

High-resolution XPS spectra registered in the binding energy range of O1*s* varied significantly after 1 and 24 h of exposure to the studied solution. The interpretation of O1*s* spectra is rather complex as the signal from several compounds can overlap. The O1*s* spectrum of the WE43 alloy surface after 1 h of corrosion in the 0.05 M NaCl solution containing 100 mM of Na_2MoO_4 was deconvoluted into three components. The first component $O_{(1)}$ located at 530.9 eV can be attributed to molybdates and/or magnesium oxide [56,66]. The second component $O_{(2)}$ at 532.0 eV was assign to magnesium carbonate or adsorbed oxygen [66,67]. The third component $O_{(3)}$ at 533.0 eV corresponds to the hydroxide, most probably in the form of $Mg(OH)_2$ [68,69], which is also supported by Raman experiments (Fig. 9). The relative ratio of $O_{(1)}$: $O_{(2)}$: $O_{(3)}$ components was 1.0 : 1.4 : 1.0. After 24 of corrosion experiments only $O_{(1)}$ and $O_{(2)}$ components with the relative ratio 2.8 : 1.0 were detected, indicating that oxides and molybdates predominate on the surface of the WE43 alloy.

3.4. Mechanism of corrosion and its inhibition

This section summarizes the results of the present contribution and attempts to propose the corrosion inhibition mechanism provided by aqueous molybdates towards the WE43 alloy.

The mechanism of the WE43 alloy corrosion in 0.05 M NaCl is schematically illustrated in Fig. 11. The surface of as polished WE43 alloy contains Mg_9Nd_2Y-type IMPs and α-Mg matrix (Fig. 11Ia). In near-neutral solutions containing NaCl, the surface of as polished WE43 Mg alloy, containing Mg_9Nd_2Y-type IMPs distributed in α-Mg matrix (Fig. 11Ia), suffers from severe corrosion attack owing to its highly negative standard potential ($E^0_{Mg^{2+}/Mg} = -2.37$ V vs. SHE). Numerous reports discuss the exact mechanism of Mg ionization [4,57,70,71],

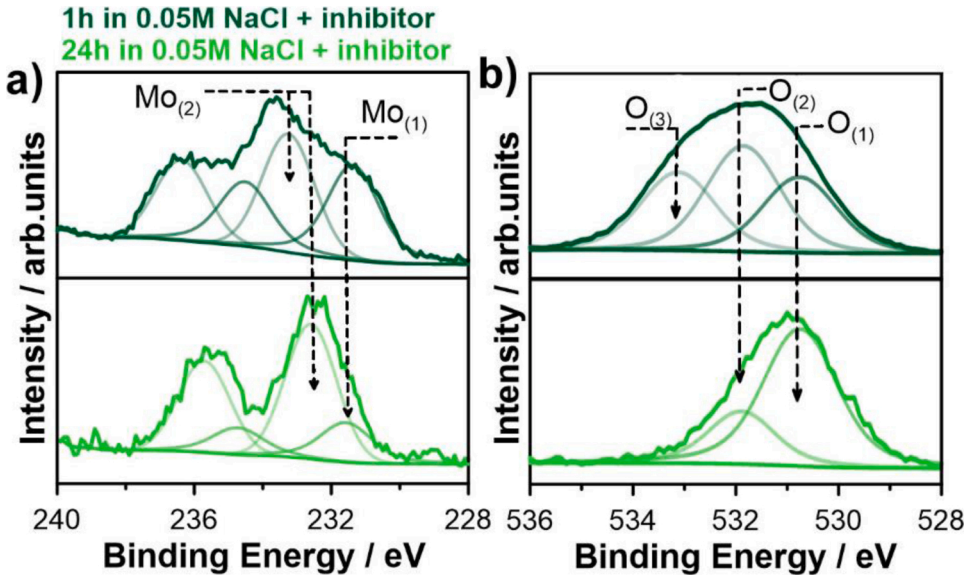

Fig. 10. High-resolution XPS spectra registered in the binding energy range of (a) Mo3d and (b) O1 s at the surface of WE43 alloy after immersion in 0.05 M NaCl +100 mM Na_2MoO_4 solution for 1 h and 24 h.

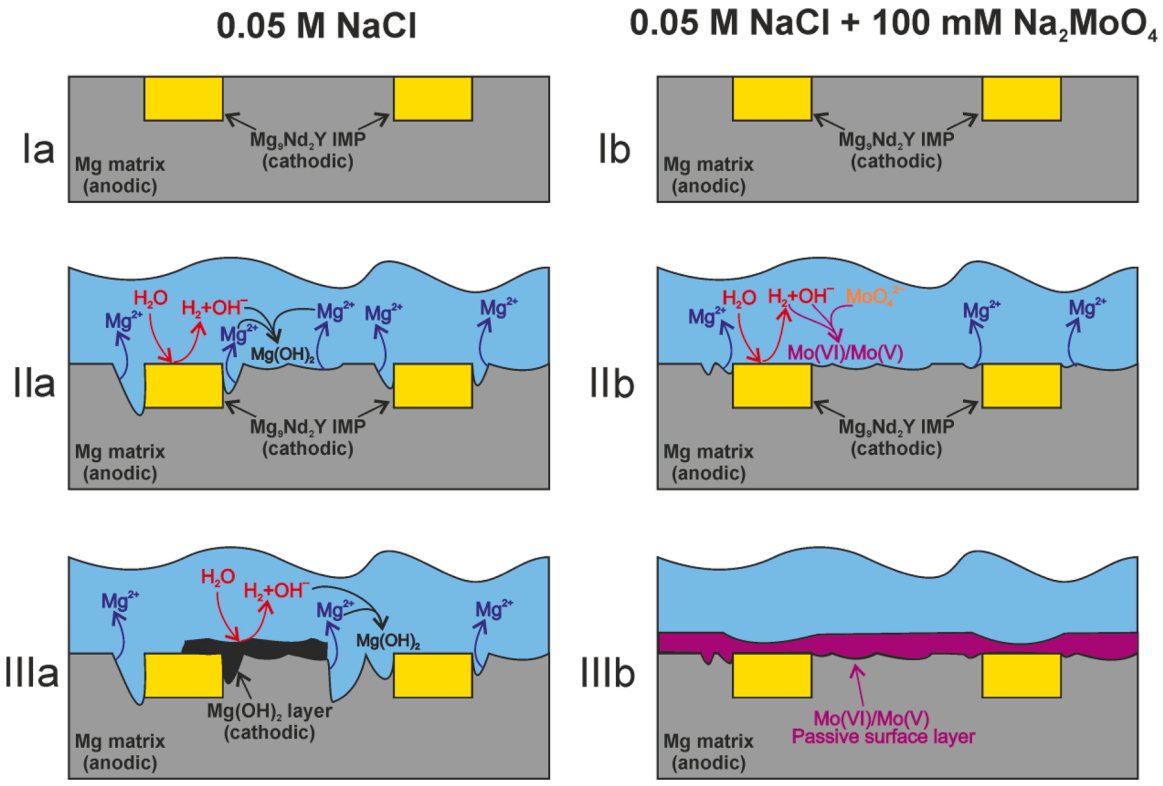

Fig. 11. Schematic illustration of the WE43 alloy corrosion in 0.05 M NaCl solution (to the left) and corrosion inhibition provided by 100 mM of aqueous molybdate (to the right).

which generally is expressed by the following reactions:

$$Mg \rightarrow Mg^{2+} + 2e^{-}; \quad (5)$$

$$2H_2O + 2e^{-} \rightarrow H_2 + 2OH^{-}; \quad (6)$$

$$Mg^{2+} + 2OH^{-} \rightarrow Mg(OH)_2. \quad (7)$$

Eqs. (5) and (6) describe electrochemical anodic and cathodic reactions, respectively, while process (7) is of chemical nature. The overall reaction in this case is:

$$Mg + 2H_2O \rightarrow Mg(OH)_2 + H_2. \quad (8)$$

In the case of the WE43 alloy, our SKPFM data (Fig. 2) show that Mg_9Nd_2Y-type IMPs found in the microstructure (EDX maps shown in Fig. 1) will initially serve as local cathodes where reaction (6) may be expected to predominantly occur (Fig. 11Ib). However, the SEM data (Fig. 6a–f) suggest that active anodic dissolution of the Mg matrix following reaction (5) readily occurs, which may reduce the relative contribution of local galvanic Mg–IMP coupling to the total corrosion process. In this case, release of Mg^{2+} into the corrosion medium leads to rapid interaction with OH^- ions (Eq. (6)) and precipitation of $Mg(OH)_2$ on the alloy surface. Such deposits are known to appear as dark regions on the surface [57], clearly seen in the light microscopy images in Fig. 8a and identified as severely corroded areas during SEM observations (Fig. 6d–f). The surface area of these dark regions is much larger than that of the IMPs, which makes the former the predominant cathodic areas [57] (Fig. 11IIIa). For this reason, the main corrosion attack occurs at the interface between dark regions and the alloy matrix, with further spreading of the dark surface area over the WE43 surface (Fig. 11IIIa) [72,73].

Our results demonstrate that the introduction of Na_2MoO_4 into 0.05 M NaCl solution dramatically changes the corrosion behaviour of the WE43 alloy. Dissolved molybdates retard corrosion attack by forming a protective insoluble film on the metal surface. Moreover, according to the electrochemical data (Figs. 4 and 5), it is essential to achieve a "critical" concentration of molybdate inhibitor in the electrolyte to provide high inhibition effectiveness. For the WE43 alloy in the examined corrosive medium this initial concentration of Na_2MoO_4 was found to be 100 mM. In turn, molybdate added in concentrations insufficient to form a stable passive layer covering all active surface areas may rather accelerate than reduce corrosion attack. In this case, only partial surface coverage results in formation of additional cathodic areas, which cause severe local corrosion. That is clearly seen in the case of 5 and 10 mM of added Na_2MoO_4, for which very low or even negative *IE*s were observed. Below, we discuss the case with a concentration of the molybdate inhibitor in the system high enough to provide corrosion inhibition.

Evidently, the first stage in the corrosion inhibition mechanism is the competitive adsorption of molybdate and chloride anions on the WE43 surface (Fig. 11IIb). The aqueous molybdate speciation is rather complex with poly- and monomolybdates present in acidic and alkaline media, respectively [29,74]. The bulk pH of as-prepared NaCl solutions with 100–150 mM of molybdate is about 7.5. It is known that the pH in the near-electrode area during corrosion of Mg alloys is alkaline (up to pH 9.5 [75–78]) due to the occurrence of reaction (6) and partial dissolution of $Mg(OH)_2$ formed according to Eq. (7) by reactions [4]:

$$Mg(OH)2 \rightleftarrows MgOH^{+} + OH^{-}; \quad (9)$$

$$MgOH^{+} \rightleftarrows Mg^{2+} + OH^{-}. \quad (10)$$

Since the medium is alkaline, only monomolybdates MoO_4^{2-} can initially adsorb on the surface. The isoelectric point (IEP) of MgO, which is covering the surface of WE43 is higher than 13 [79], while for $Mg(OH)_2$ IEP is around 10.8 [80]. Studies have shown that the pH will not reach such high values, especially in the first hours of corrosion attack [78,81]. The bulk pH of 0.05 M NaCl +100 mM Na_2MoO_4 solution after 1 h of the WE43 alloy exposure was found to be ca. 8.3–8.5. It means that the surface of the WE43 alloy in the studied media will be positively charged. This promotes adsorption of negatively charged monomolybdate anions from

the solution on the metallic surface.

Molybdates have rather low oxidizing capacity in alkaline solutions and they are thus not expected to be reduced [29,82]. Nevertheless, XPS data (Fig. 10) showed that the top surface layer is partially reduced to Mo(V) species. This is consistent with a dark colour of the passive layer. Moreover, our Raman data (Fig. 9b) confirmed that after 1 h of the WE43 alloy exposure to 0.05 M NaCl with 100 mM Na_2MoO_4, the main components of the surface passive film are $Mo_7O_{24}^{6-}$ and $Mo_8O_{26}^{4-}$ polymolybdates. After 24 h, additional peaks from dimolybdate were observed. Polymerization of adsorbed MoO_4^{2-} anions most probably proceeds as a next step in the inhibition mechanism [63,64]. At first, isolated molybdate monomers are adsorbed on the surface. Due to the high bulk concentration of molybdate ions, adsorption of excess molybdate would result in formation of hydrated polymolybdates through condensation reactions of monomers on adjacent surface sites. Note that the studied metal surface is not homogeneous, thus clustering of polymolybdates may occur far before a uniform monolayer of adsorbed MoO_4^{2-} will be achieved.

The hydrogen formed during water reduction, Eq. (6), is a strong reductant and can partially reduce initially adsorbed MoO_4^{2-} according to the reactions:

$$MoO_4^{2-} + 2H_2O + e^- \rightarrow MoO_2^+ + 4OH^-; \quad (11)$$

$$H_2 + 2OH^- - 2e^- \rightarrow 2H_2O; \quad (12)$$

$$2MoO_4^{2-} + 2H_2O + H_2 \rightarrow 2MoO_2^+ + 6OH^-. \quad (13)$$

Moreover, metallic magnesium itself is a strong reducing agent and thermodynamic calculations show that it can reduce MoO_4^{2-} up to metallic Mo [82]. However, a partial reduction of Mo(VI) to Mo(V) is more favourable under the examined conditions:

$$Mg + 2OH^- - 2e^- = Mg(OH)_2; \quad (14)$$

$$MoO_4^{2-} + 2H_2O + e^- \rightarrow MoO_2^+ + 4OH^-; \quad (15)$$

$$2MoO_4^{2-} + Mg + 4H_2O \rightarrow 2MoO_2^+ + Mg(OH)_2 + 6OH^-. \quad (16)$$

In the next step, MoO_2^+ ions can chemically react with OH^- in the near interface area, forming insoluble brown-coloured hydroxide:

$$MoO_2^+ + OH^- + H_2O \rightarrow MoO(OH)_3\downarrow. \quad (17)$$

Another possible mechanism involves formation of mixed-valence Mo(V)–Mo(VI) polymeric compounds of variable stoichiometry, known as molybdenum blues [62,74]:

$$nMoO_2^+ + MoO_4^{2-} + 2H_2O \rightarrow [Mo^{VI}O_6(Mo^{V}O_2)_n]^{n-6} + 4H^+. \quad (18)$$

The formed H^+ ions can be consumed during monomolybdate polymerization (Fig. 11IIIb). At the same time, this process shifts the chemical equilibrium of reaction (18) to the left, thus promoting further formation of mix-valenced polymolybdate species.

4. Conclusions

In this work, the effect of molybdate on the corrosion properties of the WE43 magnesium alloy was examined. High corrosion protection effectiveness of molybdate at sufficiently high concentrations (100 mM) was observed and correlated with the surface film composition. The following conclusions can be drawn:

1 The microstructure of the WE43 magnesium alloy consists of micrometer-sized Mg_9Nd_2Y-type IMPs distributed in the α-Mg matrix. SKPFM measurements confirmed cathodic electrochemical activity of these IMPs.

2 Electrochemical data revealed that aqueous molybdate at high concentrations leads to a significant decrease (up to 95 %) in the corrosion rate of the WE43 alloy in 0.05 M NaCl solutions. The optimal concentration of Na_2MoO_4 is 100 mM. Smaller concentrations increase the corrosion rate by only partial surface passivation. Concentrations above 100 mM may cause formation of microcracks in the passivating layer.

3 Raman and XPS surface analysis indicated that the molybdate inhibitor forms a protective surface film over the surface of the alloy. The resulting passivating film consists of polymerized Mo(VI) and mix-valence Mo(VI)–Mo(V) layers.

4 The mechanism of corrosion attack over the WE43 surface in 0.05 M NaCl solution is based on the initial dissolution of Mg, followed by passivation of the surface. Corrosion inhibition by Na_2MoO_4 is achieved by the competitive adsorption of molybdate anions on the surface of WE43 with formation of a Mo(VI)-Mo(V) mixed-valence protective layer, which suppresses further corrosion attack.

Data availability

The raw/processed data required to reproduce the findings of this study are available from the corresponding authors upon reasonable request.

CRediT authorship contribution statement

Dmitry S. Kharitonov: Conceptualization, Methodology, Investigation, Data curation, Formal analysis, Visualization, Validation, Funding acquisition, Project administration, Writing - original draft. **Małgorzata Zimowska:** Investigation, Writing - review & editing. **Jacek Ryl:** Investigation, Formal analysis. **Artur Zieliński:** Investigation. **Maria A. Osipenko:** Investigation. **Janusz Adamiec:** Resources, Validation. **Angelika Wrzesińska:** Investigation. **Per M. Claesson:** Validation, Writing - review & editing. **Irina I. Kurilo:** Project administration, Writing - review & editing.

Declaration of Competing Interest

The authors report no declarations of interest.

Acknowledgements

Dmitry Kharitonov gratefully acknowledges financial support from the National Science Centre (Poland) under research Grant Miniatura no. 2019/03/X/ST4/00749.

References

[1] E. Bütev Öcal, Z. Esen, K. Aydınol, A.F. Dericioğlu, Comparison of the short and long-term degradation behaviors of as-cast pure Mg, AZ91 and WE43 alloys, Mater. Chem. Phys. 241 (2020), 122350, https://doi.org/10.1016/j.matchemphys.2019.122350.

[2] H.S. Jiang, M.Y. Zheng, X.G. Qiao, K. Wu, Q.Y. Peng, S.H. Yang, Y.H. Yuan, J. H. Luo, Microstructure and mechanical properties of WE43 magnesium alloy fabricated by direct-chill casting, Mater. Sci. Eng. A 684 (2017) 158–164, https://doi.org/10.1016/j.msea.2016.11.009.

[3] J. Song, J. She, D. Chen, F. Pan, Latest research advances on magnesium and magnesium alloys worldwide, J. Magnes. Alloy 8 (2020) 1–41, https://doi.org/10.1016/j.jma.2020.02.003.

[4] M. Esmaily, J.E. Svensson, S. Fajardo, N. Birbilis, G.S. Frankel, S. Virtanen, R. Arrabal, S. Thomas, L.G. Johansson, Fundamentals and advances in magnesium alloy corrosion, Prog. Mater. Sci. 89 (2017) 92–193, https://doi.org/10.1016/j.pmatsci.2017.04.011.

[5] R. Arrabal, E. Matykina, F. Viejo, P. Skeldon, G.E. Thompson, Corrosion resistance of WE43 and AZ91D magnesium alloys with phosphate PEO coatings, Corros. Sci. 50 (2008) 1744–1752, https://doi.org/10.1016/j.corsci.2008.03.002.

[6] F. Witte, The history of biodegradable magnesium implants: a review, Acta Biomater. 6 (2010) 1680–1692, https://doi.org/10.1016/j.actbio.2010.02.028.

[7] N. Pulido-González, B. Torres, M.L. Zheludkevich, J. Rams, High Power Diode Laser (HPDL) surface treatments to improve the mechanical properties and the

corrosion behaviour of Mg-Zn-Ca alloys for biodegradable implants, Surf. Coat. Technol. 402 (2020), 126314, https://doi.org/10.1016/j.surfcoat.2020.126314.
[8] A. Soltan, M.S. Dargusch, Z. Shi, D. Gerrard, A. Atrens, Understanding the corrosion behaviour of the magnesium alloys EV31A, WE43B, and ZE41A, Mater. Corros. 70 (2019) 1527–1552, https://doi.org/10.1002/maco.201910845.
[9] P. Nowak, M. Mosiałek, D.S. Kharitonov, J. Adamiec, A. Turowska, Effect of TIG welding and rare earth elements alloying on corrosion resistance of magnesium alloys, J. Electrochem. Soc. 167 (2020), 131504, https://doi.org/10.1149/1945-7111/abb97e.
[10] W.C. Neil, M. Forsyth, P.C. Howlett, C.R. Hutchinson, B.R.W. Hinton, Corrosion of heat treated magnesium alloy ZE41, Corros. Sci. 53 (2011) 3299–3308, https://doi.org/10.1016/j.corsci.2011.06.005.
[11] Y.J. Feng, L. Wei, X.B. Chen, M.C. Li, Y.F. Cheng, Q. Li, Unexpected cathodic role of Mg41Sm5 phase in mitigating localized corrosion of extruded Mg-Sm-Zn-Zr alloy in NaCl solution, Corros. Sci. 159 (2019), 108133, https://doi.org/10.1016/j.corsci.2019.108133.
[12] S. Tang, T. Xin, W. Xu, D. Miskovic, G. Sha, Z. Quadir, S. Ringer, K. Nomoto, N. Birbilis, M. Ferry, Precipitation strengthening in an ultralight magnesium alloy, Nat. Commun. 10 (2019), https://doi.org/10.1038/s41467-019-08954-z.
[13] Z. Hu, R.L. Liu, S.K. Kairy, X. Li, H. Yan, N. Birbilis, Effect of Sm additions on the microstructure and corrosion behavior of magnesium alloy AZ91, Corros. Sci. 149 (2019) 144–152, https://doi.org/10.1016/j.corsci.2019.01.024.
[14] K. Gusieva, C.H.J. Davies, J.R. Scully, N. Birbilis, Corrosion of magnesium alloys: the role of alloying, Int. Mater. Rev. 60 (2015) 169–194, https://doi.org/10.1179/1743280414Y.0000000046.
[15] S.M. Baek, S.Y. Lee, J.C. Kim, J. Kwon, H. Jung, S. Lee, K.S. Lee, S.S. Park, Role of trace additions of Mn and Y in improving the corrosion resistance of Mg–3Al–1Zn alloy, Corros. Sci. 178 (2021), 108998, https://doi.org/10.1016/j.corsci.2020.108998.
[16] M. Deng, L. Wang, D. Höche, S.V. Lamaka, C. Wang, D. Snihirova, Y. Jin, Y. Zhang, M.L. Zheludkevich, Approaching "stainless magnesium" by Ca micro-alloying, Mater. Horizons 8 (2021) 589–596, https://doi.org/10.1039/D0MH01380C.
[17] S. Pommiers, J.Ó. Frayret, A. Castetbon, M. Potin-Gautier, Alternative conversion coatings to chromate for the protection of magnesium alloys, Corros. Sci. 84 (2014) 135–146, https://doi.org/10.1016/j.corsci.2014.03.021.
[18] X.B. Chen, N. Birbilis, T.B. Abbott, Review of corrosion-resistant conversion coatings for magnesium and its alloys, Corrosion 67 (2011), https://doi.org/10.5006/1.3563639, 035005-1-035005–035016.
[19] V.S. Saji, Review of rare-earth-based conversion coatings for magnesium and its alloys, J. Mater. Res. Technol. 8 (2019) 5012–5035, https://doi.org/10.1016/j.jmrt.2019.08.013.
[20] S.V. Lamaka, B. Vaghefinazari, D. Mei, R.P. Petrauskas, D. Höche, M. L. Zheludkevich, Comprehensive screening of Mg corrosion inhibitors, Corros. Sci. 128 (2017) 224–240, https://doi.org/10.1016/j.corsci.2017.07.011.
[21] Y. Chen, X. Lu, S.V. Lamaka, P. Ju, C. Blawert, T. Zhang, F. Wang, M. L. Zheludkevich, Active protection of Mg alloy by composite PEO coating loaded with corrosion inhibitors, Appl. Surf. Sci. 504 (2020), 144462, https://doi.org/10.1016/j.apsusc.2019.144462.
[22] S.V. Lamaka, D. Höche, R.P. Petrauskas, C. Blawert, M.L. Zheludkevich, A new concept for corrosion inhibition of magnesium: suppression of iron re-deposition, Electrochem. Commun. 62 (2016) 5–8, https://doi.org/10.1016/j.elecom.2015.10.023.
[23] D. Höche, C. Blawert, S.V. Lamaka, N. Scharnagl, C. Mendis, M.L. Zheludkevich, The effect of iron re-deposition on the corrosion of impurity-containing magnesium, Phys. Chem. Chem. Phys. (2015), https://doi.org/10.1039/c5cp05577f.
[24] J. Yang, C. Blawert, S.V. Lamaka, K.A. Yasakau, L. Wang, D. Laipple, M. Schieda, S. Di, M.L. Zheludkevich, Corrosion inhibition of pure Mg containing a high level of iron impurity in pH neutral NaCl solution, Corros. Sci. 142 (2018) 222–237, https://doi.org/10.1016/j.corsci.2018.07.027.
[25] D. Mercier, J. Światowska, E. Protopopoff, S. Zanna, A. Seyeux, P. Marcus, Inhibition of Mg corrosion by sulfur blocking of the hydrogen evolution reaction on Iron impurities, J. Electrochem. Soc. 167 (2020), 121504, https://doi.org/10.1149/1945-7111/abaf79.
[26] D.S. Kharitonov, C. Ornek, P.M. Claesson, J. Sommertune, I.M. Zharskii, I.I. Kurilo, J. Pan, Corrosion inhibition of aluminum alloy AA6063-T5 by vanadates: microstructure characterization and corrosion analysis, J. Electrochem. Soc. 165 (2018) C116–C126, https://doi.org/10.1149/2.0341803jes.
[27] D.S. Kharitonov, J. Sommertune, C. Örnek, J. Ryl, I.I. Kurilo, P.M. Claesson, J. Pan, Corrosion inhibition of aluminium alloy AA6063-T5 by vanadates: local surface chemical events elucidated by confocal Raman micro-spectroscopy, Corros. Sci. 148 (2019) 237–250, https://doi.org/10.1016/j.corsci.2018.12.011.
[28] D.S. Kharitonov, M.A. Osipenko, A. Wrzesińska, A.A. Kasach, I.V. Makarova, I. I. Kurilo, Protective action of sodium metavanadate against corrosion of AD31 aluminum alloy in neutral chloride-containing media, Russ. J. Phys. Chem. A 94 (2020) 874–879, https://doi.org/10.1134/S0036024420040068.
[29] D.S. Kharitonov, I. Dobryden, B. Sefer, J. Ryl, A. Wrzesińska, I.V. Makarova, I. Bobowska, I.I. Kurilo, P.M. Claesson, Surface and corrosion properties of AA6063-T5 aluminum alloy in molybdate-containing sodium chloride solutions, Corros. Sci. 171 (2020), 108658, https://doi.org/10.1016/j.corsci.2020.108658.
[30] Z. Feng, B. Hurley, J. Li, R. Buchheit, Corrosion inhibition study of aqueous vanadate on Mg alloy AZ31, J. Electrochem. Soc. 165 (2018) C94–C102, https://doi.org/10.1149/2.1171802jes.
[31] Z. Feng, J. Li, Z. Yang, R. Buchheit, The effect of vanadate, phosphate, fluoride compounds on the aqueous corrosion of magnesium alloy AZ31 in dilute chloride solutions, Materials (Basel) 13 (2020) 1–15, https://doi.org/10.3390/ma13061325.
[32] Z. Feng, B. Hurley, M. Zhu, Z. Yang, J. Hwang, R. Buchheit, Corrosion inhibition of AZ31 Mg alloy by aqueous selenite (SeO 3 2−), J. Electrochem. Soc. 166 (2019) C520–C529, https://doi.org/10.1149/2.0911914jes.
[33] Z. Feng, C.C. Xu, D. Zhang, R. Buchheit, Corrosion protective film formation on Mg alloy AZ31 by exposure to dilute selenite solutions, Materials (Basel) 14 (2021) 286, https://doi.org/10.3390/ma14020286.
[34] A.D. Forero López, I.L. Lehr, S.B. Saidman, Anodisation of AZ91D magnesium alloy in molybdate solution for corrosion protection, J. Alloys Compd. 702 (2017) 338–345, https://doi.org/10.1016/j.jallcom.2017.01.030.
[35] S. Mu, J. Du, H. Jiang, W. Li, Composition analysis and corrosion performance of a Mo-Ce conversion coating on AZ91 magnesium alloy, Surf. Coat. Technol. 254 (2014) 364–370, https://doi.org/10.1016/j.surfcoat.2014.06.044.
[36] T. Ishizaki, Y. Masuda, K. Teshima, Composite film formed on magnesium alloy AZ31 by chemical conversion from molybdate/phosphate/fluorinate aqueous solution toward corrosion protection, Surf. Coat. Technol. 217 (2013) 76–83, https://doi.org/10.1016/j.surfcoat.2012.11.076.
[37] L. Pezzato, K. Brunelli, E. Napolitani, M. Magrini, M. Dabalà, Surface properties of AZ91 magnesium alloy after PEO treatment using molybdate salts and low current densities, Appl. Surf. Sci. 357 (2015) 1031–1039, https://doi.org/10.1016/j.apsusc.2015.09.107.
[38] Z. Yong, J. Zhu, C. Qiu, Y. Liu, Molybdate/phosphate composite conversion coating on magnesium alloy surface for corrosion protection, Appl. Surf. Sci. 255 (2008) 1672–1680, https://doi.org/10.1016/j.apsusc.2008.04.095.
[39] I.L. Lehr, S.B. Saidman, Corrosion protection of AZ91D magnesium alloy by a cerium-molybdenum coating-The effect of citric acid as an additive, J. Magnes. Alloy 6 (2018) 356–365, https://doi.org/10.1016/j.jma.2018.10.002.
[40] Y. Song, D. Shan, R. Chen, E. Han, An environmentally friendly molybdate/phosphate black film on Mg–Zn–Y–Zr alloy, Surf. Coat. Technol. 204 (2010) 3182–3187, https://doi.org/10.1016/j.surfcoat.2010.03.006.
[41] L. Xu, C. Liu, Y. Wan, X. Wang, H. Xiao, Effects of heat treatments on microstructures and mechanical properties of Mg–4Y–2.5Nd–0.7Zr alloy, Mater. Sci. Eng. A 558 (2012) 1–6, https://doi.org/10.1016/j.msea.2012.06.085.
[42] P. Schmutz, G.S. Frankel, Characterization of AA2024-T3 by scanning kelvin probe force microscopy, J. Electrochem. Soc. 145 (1998) 2285–2295, https://doi.org/10.1149/1.1838633.
[43] D.S. Kharitonov, C. Ornek, P.M. Claesson, J. Sommertune, I.M. Zharskii, I.I. Kurilo, J. Pan, Corrosion inhibition of aluminum alloy AA6063-T5 by vanadates: microstructure characterization and corrosion analysis, J. Electrochem. Soc. 165 (2018) C116–C126, https://doi.org/10.1149/2.0341803jes.
[44] D.S. Kharitonov, I.B. Dobryden, B. Sefer, I.M. Zharskii, P.M. Claesson, I.I. Kurilo, Corrosion of AD31 (AA6063) alloy in chloride-containing solutions, Prot. Met. Phys. Chem. Surf. 54 (2018) 291–300, https://doi.org/10.1134/S2070205118020077.
[45] Z. Hu, Z. Yin, Z. Yin, K. Wang, Q. Liu, P. Sun, H. Yan, H. Song, C. Luo, H. Guan, C. Luc, Corrosion behavior characterization of as extruded Mg-8Li-3Al alloy with minor alloying elements (Gd, Sn and Cu) by scanning Kelvin probe force microscopy, Corros. Sci. 176 (2020), 108923, https://doi.org/10.1016/j.corsci.2020.108923.
[46] A.E. Coy, F. Viejo, P. Skeldon, G.E. Thompson, Susceptibility of rare-earth-magnesium alloys to micro-galvanic corrosion, Corros. Sci. 52 (2010) 3896–3906, https://doi.org/10.1016/j.corsci.2010.08.006.
[47] A.D. King, N. Birbilis, J.R. Scully, Accurate electrochemical measurement of magnesium corrosion rates; a combined impedance, mass-loss and hydrogen collection study, Electrochim. Acta 121 (2014) 394–406, https://doi.org/10.1016/j.electacta.2013.12.124.
[48] H. Torbati-Sarraf, S.A. Torbati-Sarraf, A. Poursaee, T.G. Langdon, Electrochemical behavior of a magnesium ZK60 alloy processed by high-pressure torsion, Corros. Sci. 154 (2019) 90–100, https://doi.org/10.1016/j.corsci.2019.04.006.
[49] A. Soltan, M.S. Dargusch, Z. Shi, D. Gerrard, S. Al Shabibi, Y. Kuo, A. Atrens, Corrosion of Mg alloys EV31A, WE43B, and ZE41A in chloride- and sulfate-containing solutions saturated with magnesium hydroxide, Mater. Corros. 71 (2020) 956–979, https://doi.org/10.1002/maco.201911375.
[50] G. Song, A. Atrens, D.S. John, X. Wu, J. Nairn, The anodic dissolution of magnesium in chloride and sulphate solutions, Corros. Sci. 39 (1997) 1981–2004, https://doi.org/10.1016/S0010-938X(97)00090-5.
[51] G. Baril, G. Galicia, C. Deslouis, N. Pébère, B. Tribollet, V. Vivier, An impedance investigation of the mechanism of pure magnesium corrosion in sodium sulfate solutions, J. Electrochem. Soc. 154 (2007) C108–C113, https://doi.org/10.1149/1.2401056.
[52] G. Baril, N. Pébère, Corrosion of pure magnesium in aerated and deaerated sodium sulphate solutions, Corros. Sci. 43 (2001) 471–484, https://doi.org/10.1016/S0010-938X(00)00095-0.
[53] S. Feliu, Electrochemical impedance spectroscopy for the measurement of the corrosion rate of magnesium alloys: brief review and challenges, Metals (Basel) 10 (2020) 1–23, https://doi.org/10.3390/met10060775.
[54] M.P. Gomes, I. Costa, N. Pébère, J.L. Rossi, B. Tribollet, V. Vivier, On the corrosion mechanism of Mg investigated by electrochemical impedance spectroscopy, Electrochim. Acta 306 (2019) 61–70, https://doi.org/10.1016/j.electacta.2019.03.080.
[55] B.A. Boukamp, A linear Kronig-Kramers transform test for immittance data validation, J. Electrochem. Soc. 142 (1995) 1885–1894, https://doi.org/10.1149/1.2044210.

[56] H. Verbruggen, K. Baert, H. Terryn, I. De Graeve, Molybdate-phosphate conversion coatings to protect steel in a simulated concrete pore solution, Surf. Coat. Technol. 361 (2019) 280–291, https://doi.org/10.1016/j.surfcoat.2018.09.056.
[57] S. Thomas, N.V. Medhekar, G.S. Frankel, N. Birbilis, Corrosion mechanism and hydrogen evolution on Mg, Curr. Opin. Solid State Mater. Sci. 19 (2015) 85–94, https://doi.org/10.1016/j.cossms.2014.09.005.
[58] A. Maltseva, V. Shkirskiy, G. Lefèvre, P. Volovitch, Effect of pH on Mg(OH)2 film evolution on corroding Mg by in situ kinetic Raman mapping (KRM), Corros. Sci. 153 (2019) 272–282, https://doi.org/10.1016/j.corsci.2019.03.024.
[59] Y.M. Yan, A. Maltseva, P. Zhou, X.J. Li, Z.R. Zeng, O. Gharbi, K. Ogle, M. La Haye, M. Vaudescal, M. Esmaily, N. Birbilis, P. Volovitch, On the in-situ aqueous stability of an Mg-Li-(Al-Y-Zr) alloy: role of Li, Corros. Sci. 164 (2020), 108342, https://doi.org/10.1016/j.corsci.2019.108342.
[60] A. Maltseva, S.V. Lamaka, K.A. Yasakau, D. Mei, D. Kurchavov, M.L. Zheludkevich, G. Lefèvre, P. Volovitch, In situ surface film evolution during Mg aqueous corrosion in presence of selected carboxylates, Corros. Sci. 171 (2020), 108484, https://doi.org/10.1016/j.corsci.2020.108484.
[61] P. Dawson, C.D. Hadfield, G.R. Wilkinson, The polarized infra-red and Raman spectra of Mg(OH)2 and Ca(OH)2, J. Phys. Chem. Solids 34 (1973) 1217–1225, https://doi.org/10.1016/S0022-3697(73)80212-4.
[62] K.-H. Tytko, Gmelin Handbook of Inorganic Chemistry. Mo Molybdenum, Springer Berlin Heidelberg, Berlin, Heidelberg, 1986, https://doi.org/10.1007/978-3-662-08837-1.
[63] P.A. Spevack, N.S. McIntyre, A Raman and XPS investigation of supported molybdenum oxide thin films. 1. Calcination and reduction studies, J. Phys. Chem. 97 (1993) 11020–11030, https://doi.org/10.1021/j100144a020.
[64] H. Hu, I.E. Wachs, S.R. Bare, Surface structures of supported molybdenum oxide catalysts: characterization by Raman and Mo L3-edge XANES, J. Phys. Chem. 99 (1995) 10897–10910.
[65] M. Wang, J. You, A.A. Sobol, J. Wang, J. Wu, X. Lv, Temperature-dependent Raman spectroscopic studies of microstructure present in dipotassium molybdate crystals and their melts, J. Raman Spectrosc. 47 (2016) 1259–1265, https://doi.org/10.1002/jrs.4948.
[66] J.-G. Choi, L.T. Thompson, XPS study of as-prepared and reduced molybdenum oxides, Appl. Surf. Sci. 93 (1996) 143–149, https://doi.org/10.1016/0169-4332(95)00317-7.
[67] V. Rheinheimer, C. Unluer, J. Liu, S. Ruan, J. Pan, P. Monteiro, XPS study on the stability and transformation of hydrate and carbonate phases within MgO systems, Materials (Basel) 10 (2017) 75, https://doi.org/10.3390/ma10010075.
[68] H. Yao, Y. Li, A.T. Wee, An XPS investigation of the oxidation/corrosion of melt-spun Mg, Appl. Surf. Sci. 158 (2000) 112–119, https://doi.org/10.1016/S0169-4332(99)00593-0.
[69] A.I. Ikeuba, B. Zhang, J. Wang, E.-H. Han, W. Ke, P.C. Okafor, SVET and SIET study of galvanic corrosion of Al/MgZn 2 in aqueous solutions at different pH, J. Electrochem. Soc. 165 (2018) C180–C194, https://doi.org/10.1149/2.0861803jes.
[70] A. Atrens, G.L. Song, F. Cao, Z. Shi, P.K. Bowen, Advances in Mg corrosion and research suggestions, J. Magnes. Alloy 1 (2013) 177–200, https://doi.org/10.1016/j.jma.2013.09.003.
[71] A. Atrens, G.L. Song, M. Liu, Z. Shi, F. Cao, M.S. Dargusch, Review of recent developments in the field of magnesium corrosion, Adv. Eng. Mater. 17 (2015) 400–453, https://doi.org/10.1002/adem.201400434.
[72] N. Birbilis, A.D. King, S. Thomas, G.S. Frankel, J.R. Scully, Evidence for enhanced catalytic activity of magnesium arising from anodic dissolution, Electrochim. Acta 132 (2014) 277–283, https://doi.org/10.1016/j.electacta.2014.03.133.
[73] M. Curioni, The behaviour of magnesium during free corrosion and potentiodynamic polarization investigated by real-time hydrogen measurement and optical imaging, Electrochim. Acta 120 (2014) 284–292, https://doi.org/10.1016/j.electacta.2013.12.109.
[74] E.A. Nagul, I.D. McKelvie, P. Worsfold, S.D. Kolev, The molybdenum blue reaction for the determination of orthophosphate revisited: opening the black box, Anal. Chim. Acta 890 (2015) 60–82, https://doi.org/10.1016/j.aca.2015.07.030.
[75] S.S. Jamali, S.E. Moulton, D.E. Tallman, M. Forsyth, J. Weber, G.G. Wallace, Applications of scanning electrochemical microscopy (SECM) for local characterization of AZ31 surface during corrosion in a buffered media, Corros. Sci. 86 (2014) 93–100, https://doi.org/10.1016/j.corsci.2014.04.035.
[76] J. Izquierdo, L. Nagy, I. Bitter, R.M. Souto, G. Nagy, Potentiometric scanning electrochemical microscopy for the local characterization of the electrochemical behaviour of magnesium-based materials, Electrochim. Acta 87 (2013) 283–293, https://doi.org/10.1016/j.electacta.2012.09.029.
[77] S.V. Lamaka, G. Knörnschild, D.V. Snihirova, M.G. Taryba, M.L. Zheludkevich, M. G.S. Ferreira, Complex anticorrosion coating for ZK30 magnesium alloy, Electrochim. Acta 55 (2009) 131–141, https://doi.org/10.1016/j.electacta.2009.08.018.
[78] S.V. Lamaka, J. Gonzalez, D. Mei, F. Feyerabend, R. Willumeit-Römer, M. L. Zheludkevich, Local pH and its evolution near Mg alloy surfaces exposed to simulated body fluids, Adv. Mater. Interfaces 5 (2018), 1800169, https://doi.org/10.1002/admi.201800169.
[79] M. Kosmulski, The pH dependent surface charging and points of zero charge. VIII. Update, Adv. Colloid Interface Sci. 275 (2020), 102064, https://doi.org/10.1016/j.cis.2019.102064.
[80] H. Schott, Electrokinetic studies of magnesium hydroxide, J. Pharm. Sci. (1981), https://doi.org/10.1002/jps.2600700505.
[81] D. Mei, S.V. Lamaka, X. Lu, M.L. Zheludkevich, Selecting medium for corrosion testing of bioabsorbable magnesium and other metals – a critical review, Corros. Sci. 171 (2020), 108722, https://doi.org/10.1016/j.corsci.2020.108722.
[82] V. Shkirskiy, P. Keil, H. Hintze-Bruening, F. Leroux, T. Stimpfling, D. Dragoe, K. Ogle, P. Volovitch, MoO_4^{2-} as a soluble inhibitor for Zn in neutral and alkaline solutions, Corros. Sci. 99 (2015) 31–41, https://doi.org/10.1016/j.corsci.2015.05.005.